JGR Oceans

RESEARCH ARTICLE
10.1029/2020JC016178

Vortex and Biogeochemical Dynamics for the Hypoxia Formation Within the Coastal Transition Zone off the Pearl River Estuary

Dou Li[1], Jianping Gan[1,2], Rex Hui[1], Zhiqiang Liu[1,3], Liuqian Yu[1], Zhongming Lu[2], and Minhan Dai[4]

[1]Department of Ocean Science and Department of Mathematics, Hong Kong University of Science and Technology, Hong Kong, [2]Division of Environment and Sustainability, Hong Kong University of Science and Technology, Hong Kong, [3]Department of Ocean Science and Engineering, Southern University of Science and Technology, Shenzhen, China, [4]State Key Laboratory of Marine Environmental Science, Xiamen University, Xiamen, China

Abstract Satellite-derived chlorophyll data, in situ measurements, and time series buoy monitoring revealed the persistent and deteriorating seasonal eutrophication and hypoxia with two distinct centers in the coastal transition zone (CTZ) between the Pearl River Estuary and the adjacent continental shelf off Hong Kong. We used a process-oriented coupled physical-biogeochemical numerical model to investigate the intrinsic physical and biogeochemical dynamics under the extrinsic forcing of wind, river discharge, and tides for the hypoxia formation in the CTZ. We found that the convergence induced by cyclonic vortices in the CTZ, which were formed by the buoyancy-driven currents and wind-driven shelf currents, created the stable water column with weak mixing and long residence time and accumulated nutrients and organic matter for the eutrophication and hypoxia development. The biophysical responses to spring-neap cycle further demonstrated the coherent linkages of oceanic currents, vortex formation, and convergence of organic matter within the CTZ and indicated the critical role of mixing in the dissolved oxygen (DO) budgets during the spring-neap tidal cycle. The study found that biogeochemical substances and processes are necessary conditions for eutrophication and hypoxia formation, and when these necessary conditions are combined with the favorable hydrodynamic conditions, they form a sufficient condition for eutrophication and hypoxia formation in the CTZ.

Plain Language Summary Observations show that eutrophication and persistent hypoxia (dissolved oxygen less than 2 mg L^{-1}) existed at the bottom of the coastal transition zone (CTZ) between the Pearl River Estuary and adjacent continental shelf. We found that rich nutrients from river discharge and sufficient light stimulated the primary production, which was the necessary condition for hypoxia to form in the CTZ. Cyclonic vortices and centers of convergence in the CTZ were favorable for the accumulation of nutrients and organic matter and were characterized by longer residence time, strong stratification, and weak mixing. Combined with the necessary condition, they provided a sufficient condition for the eutrophication/hypoxia to form in the CTZ.

1. Introduction

Due to eutrophication, hypoxia (dissolved oxygen [DO] less than 2 mg L^{-1}) has frequently been observed in more than 400 coastal waters affecting a total area of more than 245,000 km^2 (Diaz & Rosenberg, 2008). Hypoxia reduces benthic biomass and disrupts the sustainability of marine ecosystem by altering community structure, phytoplankton stoichiometry, nutrient cycling, and consequently, trophic efficiency (Seitz et al., 2009).

High primary productivity induced by elevated nutrients in river plumes leads to high organic matter (OM) deposition and, subsequently, reduces the DO in the bottom layer (Testa & Kemp, 2011). Although excess nutrients and associated biogeochemical processes are well-known necessary conditions for eutrophication and hypoxia (Breitburg et al., 2018), the remaining challenge is to delineate the combined dynamics between hydrodynamic conditions and biogeochemical dynamics that provide a sufficient biophysical condition and a closure understanding for eutrophication and hypoxia formation in a complex estuarine and coastal region (Rabouille et al., 2008). Hypoxia varies in different estuarine systems because of different nutrient loading

Key Points:
- Seasonal eutrophication/hypoxia is persistently found in the coastal transition zone (CTZ) off the Pearl River Estuary
- The vortex converges nutrients and organic matter, produces a longer residence time, and stabilizes waters for the hypoxia in the CTZ
- Combinations of biogeochemical processes and unique hydrodynamics in the CTZ provide a sufficient condition for the eutrophication/hypoxia

Correspondence to:
J. Gan,
magan@ust.hk

Citation:
Li, D., Gan, J., Hui, R., Liu, Z., Yu, L., Lu, Z., & Dai, M. (2020). Vortex and biogeochemical dynamics for the hypoxia formation within the coastal transition zone off the Pearl River Estuary. *Journal of Geophysical Research: Oceans*, *125*, e2020JC016178. https://doi.org/10.1029/2020JC016178

Received 23 FEB 2020
Accepted 26 JUL 2020
Accepted article online 4 AUG 2020

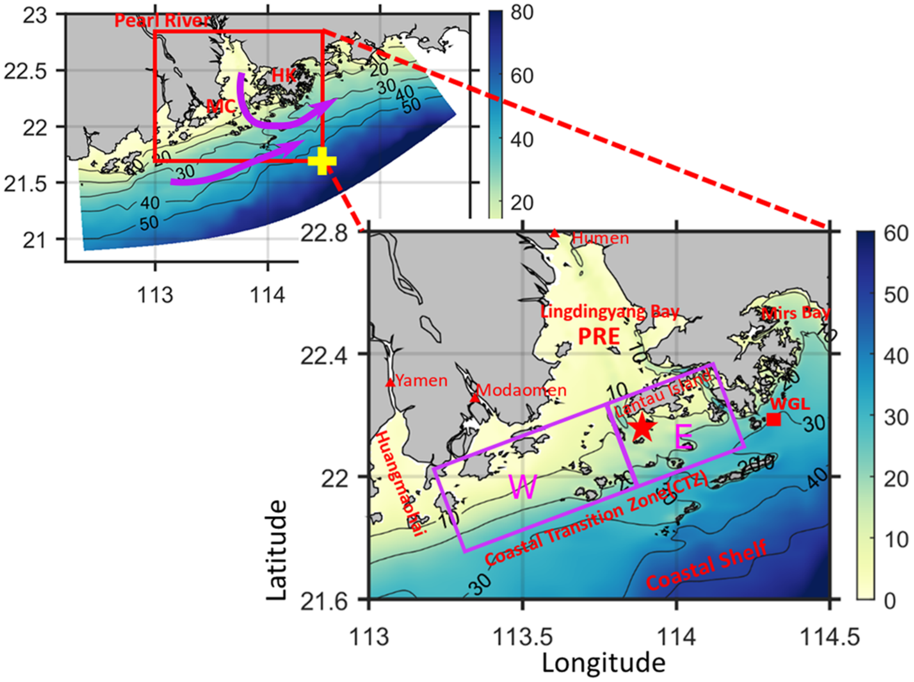

Figure 1. Map of the model domain showing topography and isobaths (in meters), and the enlarged area (enclosed in the red lines) is the Pearl River Estuary (PRE) and adjacent shelf. MC, Macao; HK, Hong Kong. Magenta arrows show the general summer circulation. W and E in the subdivided boxes represent the western and eastern coastal transition zone (CTZ). The yellow cross shows the location of Station A7. The red star denotes the location of buoy mooring station. The red square shows the location of Waglan Island (WGL). The red triangles indicate the location of Humen, Modaomen, and Yamen.

and physically forced circulations, which critically regulate transport, accumulation, and the residence time of biogeochemical substances.

Pearl River is the 17th largest river in the world and has a freshwater discharge of $2.85 \times 10^{11} \mathrm{m}^3\ \mathrm{yr}^{-1}$, and 78% of the discharge occurs during the flood season (April to September) (Dai et al., 2014). The Pearl River Estuary (PRE), surrounded by several urban centers such as Hong Kong and Macao (Figure 1), receives high concentrations of nutrients, with annual ammonia, nitrate, and phosphate loads of $(2.64 \pm 0.76) \times 10^4$ tons, $(4.30 \pm 0.67) \times 10^5$ tons, and $(2.55 \pm 0.15) \times 10^4$ tons, respectively (Governmental Report on the Marine Environmental Quality, Guangdong Province, 2013–2017).

We know that extensive biogeochemical processes such as the aerobic respiration and nitrification are the main drivers of the persistent hypoxia in the Pearl River and upper PRE (He et al., 2014). However, recent observations showed that deteriorating eutrophication/hypoxia occurred over several thousand km^2 in the coastal transition zone (CTZ) (Lu et al., 2018; Zhao et al., 2020), which is the transition region between the lower PRE and the adjacent shelf (Figure 1).

Despite the evidence that physical processes are controlling the underlying biogeochemical processes responsible for eutrophication/hypoxia, previous eutrophication/hypoxia studies in the PRE mainly focused on general biogeochemical processes regarding cycling of excess nutrients and OM over the specific region in the CTZ (Su et al., 2017; Zhao et al., 2020). However, as shown by the observed spatiotemporally varying eutrophication/hypoxia in the CTZ in Lu et al. (2018) and this study, only the combined physical and biogeochemical processes could form a sufficient condition for the development of eutrophication/hypoxia.

The hydrodynamic control of the biogeochemical processes that form eutrophication/hypoxia has been widely reported in many regional seas around the world. Vortex or rotational flow, which is mainly formed by flow-topography interaction, vortex stretching, and squashing of water column (Wu et al., 2007), generates water convergence for the accumulation of OM and for the increase of water residence time and provides a favorable condition for the formation of eutrophication and hypoxia. Ranasinghe et al. (2006) showed that strong convergence occurs over locations with unique topography (such as the salient edge of a coastal cape or the lee of islands). In these regions, nutrients and other biogeochemical substances converge because of forming vortices. Topographically sheltered seafloors were proved to be prone to hypoxia formation in the northern Baltic Sea (Virtanen et al., 2019). Other examples are the northern Gulf of Mexico, Changjiang Estuary, and Bohai Sea, where the distribution of hypoxia is closely linked with coastal shallow shoals, submerged valley, and mesoscale anticyclonic vortex, respectively (Chen et al., 2017; DiMarco et al., 2010; Wei et al., 2019). Lu et al. (2018) found that currents interacting with bottom topography regulate the distribution of OM and hypoxia in the west off the PRE. All these studies showed how important hydrodynamics are in forming hypoxia.

The circulation in the estuary-coast-shelf system around the PRE is more complex than the circulation in the Baltic Sea or the Gulf of Mexico. The circulation around the PRE is driven by the estuarine circulation in the PRE, a plume-driven offshore buoyant current, and a monsoon-driven northeastward shelf current (Figure 1). Superimposed by high-frequency tidal currents, the multiforcing currents exhibit complex patterns constrained by the local coastline and shelf topography (Zu & Gan, 2015). The seaward surface gravitational current from the PRE converges with the northeastward wind-driven shelf current and the associated shoreward geostrophic cross-shelf transport. In addition, the spring-neap tidal cycle also contributes to the changes in the vertical stratification, turbulent mixing, as well as distribution and cycling of biogeochemical substances (Zhang et al., 2007). However, despite these previous studies, the effect of the coupled physical-biogeochemical dynamics that determines eutrophication/hypoxia in coastal seas such as the CTZ off the PRE remains underinvestigated.

Most of the previous studies have been paying more attention to the biogeochemical mechanism and less to the important role of hydrodynamics in formation of eutrophication and hypoxia. Water column stability, residence time, and circulation play critical roles in the transport and accumulation of nutrients and OM for eutrophication and hypoxia. Pieces of evidence suggest that eutrophication and hypoxia cannot be achieved by biogeochemical process alone, and they are formed by coupled physical and biogeochemical processes, which is true in PRE as well as in other hypoxic zones globally (Breitburg et al., 2018; Lu et al., 2018; Rabouille et al., 2008).

In this study, we found that the unique hydrodynamics, such as vortex-induced convergence resulting from the interactions of topography with buoyancy-driven estuarine current and the wind-driven shelf current, provided a biophysical-favorable environment for the eutrophication/hypoxia formation. We utilized multiyear in situ observations and a coupled physical-biogeochemical model to identify the vortex features and their biophysical effect on hypoxia formation in the CTZ. The observations and numerical model implementations are introduced in section 2. In section 3, we use the observed data and the model results to describe the characteristic distribution and response of eutrophication/hypoxia. Biophysical dynamics of eutrophication/hypoxia formation are described in section 5. In section 5, we illustrate the dynamics further by examining how the hypoxia responds to the varying hydrodynamic and biogeochemical processes during a spring-neap tidal cycle. Finally, the summary and conclusions are presented in section 6.

2. Observations and Ocean Model

2.1. Observed Data

For our study, we analyzed observed data collected from 10 summer cruises, a buoy monitoring station, satellite remote sensing data, river hydrometric stations, and from the Hong Kong Observatory. In this section, we describe these data.

Ten cruises (Table 1) were conducted in the PRE and over the adjacent shelf during each summer from 2014 to 2018 (Figure 2). The sampling regions covered the region from outside Huangmaohai to southeast of Hong Kong, from the vicinity of Humen to 50 m isobath over the shelf. In situ salinity, temperature, chlorophyll, and DO were measured with a calibrated Sea-Bird SBE17plus conductivity-temperature-depth (CTD) profiling system. The CTD has a precision of ±0.0005 S m^{-1} and ±0.005°C. We calibrated the DO and chlorophyll data from sensors with the onboard or laboratory measurements, of which DO was determined onboard by the Winkler titration method and chlorophyll was measured by the standard fluorometric

Table 1
Observation Time, River Discharge Rate, and Wind Stress at Waglan Island for 10 Summer Cruises From 2014 to 2018

Cruise number	Year	Leg symbol	Period	Alongshore wind stress (Pa)	Cross-shore wind stress (Pa)	River discharge rate ($m^3 s^{-1}$)
1	2014	L1	6 Jul to 29 Jul	0.006	0.014	13,687
2	2015	L1	6 Jul to 15 Jul	−0.002	−0.005	10,812
3	2015	L2	15 Jul to 24 Jul	0.024	0.029	8,515
4	2016	L1	17 Jun to 20 Jun	0.008	0.015	37,093
5	2017	L1	11 Jul to 22 Jul	−0.027	−0.007	28,328
6	2017	L2	22 Jul to 28 Jul	−0.029	−0.017	17,250
7	2017	L3	28 Jul to 30 Jul	0.003	−0.003	12,389
8	2018	L1	6 Jul to 14 Jul	−0.028	−0.012	12,012
9	2018	L2	20 Jul to 25 Jul	−0.013	0.007	7,074
10	2018	L3	28 Jul to 31 Jul	0.011	0.013	8,369

method (Parsons, 2013). Nutrient samples were run on a Technicon AA3 Auto-Analyzer (BranLube, GmbH), and nitrate was analyzed using the copper-cadmium column reduction method as previously described (Han et al., 2012) with a detection limit of 0.1 $\mu mol\ L^{-1}$.

In addition to the cruise data, we used data from a real-time marine monitoring buoy system deployed at a water depth of 12 m south of Hong Kong waters (22.153°N, 113.900°E, Figure 1). The buoy had a HydroCAT-EP that collected the temperature, salinity, and DO every 15 min at the surface, middle, and bottom layers. The buoy also had downward-looking ADCP that measured velocity at 1-m vertical bins (https://ocean.ust.hk/progress-and-update/real-time-observation/). Hourly-smoothed buoy data between 1 July 2018 and 6 July 2018 were used to examine the variation of water column stability, vertical shear, and DO from the spring tide to neap tide.

Long-term summer surface chlorophyll was examined by the data derived from high-resolution (4 km) merged L3 Ocean Color products (Saulquin et al., 2010) from 1998 to 2018 (http://www.globcolour.info/).

We obtained daily Pearl River discharge rate at hydrological stations covering streams of total river flow entering the PRE from the Information Center of Water Resources (Bureau of Hydrology, the Ministry of Water Resources of PR China).

Lastly, hourly wind and water elevation data in Waglan Island (WGL; Figure 1) were obtained from the Hong Kong Observatory (https://www.hko.gov.hk/tc/cis/form/online_reqform.htm#).

2.2. Numerical Coupled Model and Implementation

The coupled physical-biogeochemical model is based on the Regional Ocean Modeling System (ROMS) (Shchepetkin & McWilliams, 2005). To link the PRE with the adjacent shelf systems, our model domain extended from 112.3°E, 20.9°N in the southwest to 114.3°E, 23.1°N in the northeast and was discretized into a matrix with 400 × 441 cells using an orthogonal curvilinear grid system (Figure 1). The grid size at the

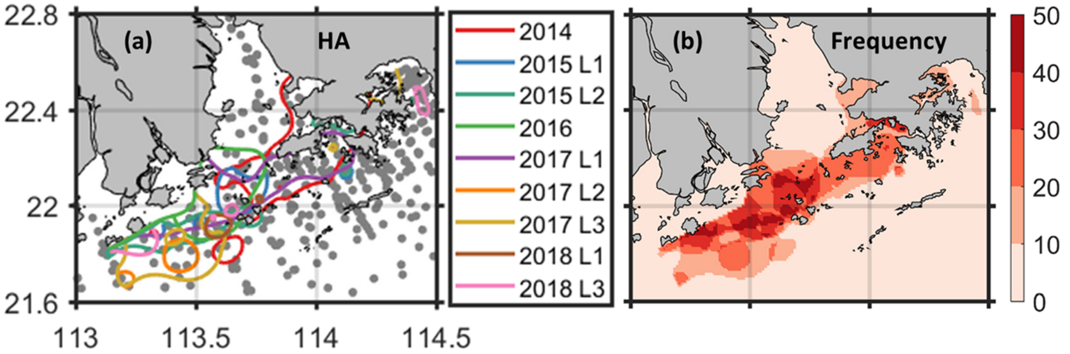

Figure 2. (a) Hypoxia area and (b) hypoxia frequency ([Hypoxia occurrences]/[Total cruises] × 100%) observed during cruises from 2014 to 2018 in the Pearl River Estuary and adjacent shelf sea. The gray points represent the sampling station locations.

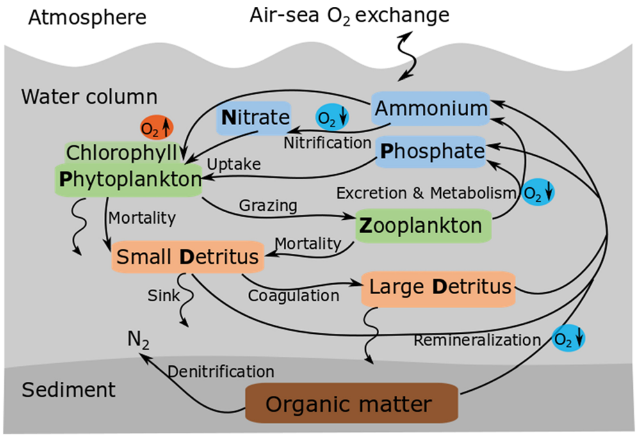

Figure 3. Schematic of the coupled nitrogen, phosphorus, phytoplankton, zooplankton, and detritus (NPPZD) in the oxygen model. Specifically, the model includes two species of inorganic nitrogen (nitrate and ammonium) and phosphate, one phytoplankton group to allow to uptake nutrient and release O_2 through photosynthesis, one functional zooplankton group to graze phytoplankton and conduct excretion and metabolism, and two pools of detritus to represent the sink and coagulation of organic matter from the mortality of phytoplankton and zooplankton. The detritus consumes O_2 and releases ammonium and phosphate through remineralization or is converted to N_2 through denitrification. The ammonium subsequently consumes O_2 and is transformed to nitrate through nitrification.

southern open boundary was ~1 km and gradually decreased to less than ~0.1 km in the estuary and inner shelf around Hong Kong. The model had 30 terrain-following vertical layers on S-coordinate, with higher resolution near the surface and the bottom. The model used a Level 2.5 turbulent closure scheme for vertical mixing provided by Mellor and Yamada (1982), a third-order upwind-biased scheme for horizontal momentum advection, and a multidimensional positive definite advection transport algorithm (MPDATA) to approximate the advection terms of tracers (Smolarkiewicz & Margolin, 1998). Details of how the model was implemented and validated are in Liu and Gan (2020).

We coupled a nitrogen, phosphorus, phytoplankton, zooplankton, and detritus (NPPZD) model (Gan et al., 2014) and a DO model (Fennel et al., 2006) to our physical model (Figure 3). In the biological model, the governing DO balance equation is expressed as

$$\begin{aligned}\text{Rate} = \text{HADV} + \text{VADV} + \text{HDIF} + \text{VDIF} + \text{Phot} + \text{Nitrif} \\ + \text{Remin} + \text{Metab} + \text{Rea} + \text{SOD}\end{aligned} \tag{1}$$

Terms on the right side of the equation represent the horizontal advection (HADV), vertical advection (VADV), horizontal diffusion (HDIF), vertical diffusion (VDIF), photosynthesis (Phot), nitrification (Nitri), metabolism (Metab), remineralization (Remin), re-aeration (Rea), and sediment oxygen demanding (SOD). We defined the biological parameters based on previous hypoxia modeling studies, especially those in the PRE (Gan et al., 2014; Lu et al., 2018).

The model was initialized with the temperature, salinity, nitrate, phosphate, DO, and chlorophyll profile data at Station A7 (Figure 1) as in Gan et al. (2010, 2014). The initial values of phytoplankton, zooplankton, and detritus were calculated from chlorophyll data by assuming the ratios of 1.59, 0.3, and 0.7 (Evans & Garçon, 1997) for chlorophyll/phytoplankton, zooplankton/phytoplankton, and detritus/phytoplankton, respectively.

In this process-oriented study aiming to identify the fundamental physical-biogeochemical response to key forcing processes of winds, buoyancy, and tides in the CTZ, we used simplified but representative forcing. A multiyear summer averaged river discharge rate, 18,400 $m^3\ s^{-1}$, was proportionally applied at eight river outlets (Lu et al., 2018). Salinity, temperature, NO_3, PO_4, and DO of the river discharge were set to 3 PSU, 28.6°C, 90 mmol m^{-3}, 1.5 mmol m^{-3}, and 3 mg L^{-1}, respectively (Cai et al., 2004). We set daily average solar radiation to 195 W m^{-2} with a diurnal cycle distribution and neglected other buoyant fluxes from atmosphere. Spatial uniform southwesterly wind stress (0.025 Pa, 23° anticlockwise from true east) that represented the typical summer monsoon was applied over the domain (Gan et al., 2009).

Tidal forcing extracted from the Oregon State University Tidal Inversion Software (OTIS) (Egbert & Erofeeva, 2002) was imposed at the open boundaries (OBs). Tidal waves from the Northwest Pacific Ocean determined the tidal currents for our study area (Zu et al., 2008). We applied a tidal-subtidal active open boundary condition (OBC) (Liu & Gan, 2016) to all physical variables along the open boundaries and a passive OBC (i.e., gradient boundary condition) to biogeochemical variables to exclude external biogeochemical fluxes beyond the PRE domain in this process-oriented study.

2.3. Physical Descriptors of Circulation

To characterize the physical properties and oceanographic features of circulation in the PRE, the circulation-related relative vorticity and divergence, stratification related buoyancy frequency, vertical shear and Richardson number, and residence time were calculated from the ROMS outputs.

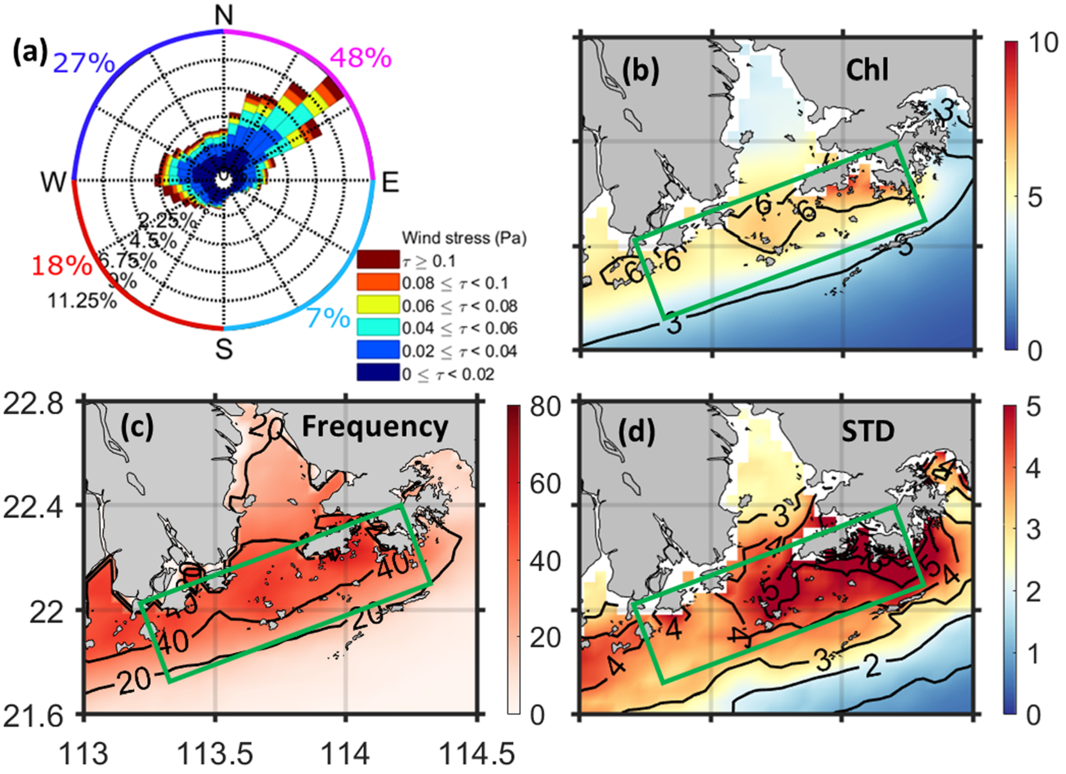

Figure 4. (a) Wind stress rose of the wind stress (Pa) measured at Waglan Island (WGL) during summer (June, July, and August) from 1998 to 2018; horizontal distributions of (b) average chlorophyll (μg L^{-1}); (c) frequency (%) of chlorophyll >5 μg L^{-1}; and (d) standard deviations (STD) of summer chlorophyll from 1998 to 2018. The chlorophyll values are derived from satellite data.

Relative vorticity ($\xi = -\frac{\partial u}{\partial y} + \frac{\partial v}{\partial x}$) and divergence ($\mathrm{DIV} = \frac{\partial u}{\partial x} + \frac{\partial v}{\partial y}$) were used to describe the local rotation and the flux of the water mass, where u and v are the eastward and northward velocity, respectively. A negative DIV means the convergence of the water mass. We described the local circulation based on Stokes's theorem: $\Gamma = \oint \vec{V} dl = \iint \xi dA$, where Γ is the circulation, $\vec{V}$ is the velocity vector, and ξ is the vertical relative vorticity. A positive Γ represents cyclonic circulation, while a negative value represents anticyclonic circulations.

The buoyancy frequency ($\mathrm{N}^2 = -\frac{g}{\rho_0}\frac{\partial \rho}{\partial z}$) and vertical velocity shear ($\mathrm{VS} = \left(\frac{\partial u}{\partial z}\right)^2 + \left(\frac{\partial v}{\partial z}\right)^2$) were used to evaluate the water column stability, where ρ_0 is the mean water density, ρ is seawater density, g is gravity acceleration, and z is the vertical coordinate with positive upwards. The gradient Richardson number ($\mathrm{RI} = \frac{-\frac{g}{\rho}\frac{\partial \rho}{\partial z}}{\left(\frac{\partial u}{\partial z}\right)^2 + \left(\frac{\partial v}{\partial z}\right)^2} = \frac{\mathrm{N}^2}{\mathrm{VS}}$) defines the ratio between the buoyancy frequency and the vertical velocity shear. The condition $\mathrm{RI} > 0.25$ indicates a stable regime (Miles, 1961).

The time that water masses stay in a specific region defines their residence time for the region. We used a parcel-tracking Euler technique (Liu & Gan, 2017) to record residence time of water masses in the PRE.

3. Observed Biogeochemical Features

3.1. Mean Characteristics

The statistical characteristics of the summer wind stress measured at 10 m above the surface at WGL Station from 1998 to 2018 are shown in Figure 4a. The prevailing southwesterly wind occurred for 48%

of the summer. The distribution of long-term (1998 to 2018) satellite-derived summer averaged chlorophyll (Figure 4b) and frequency of high chlorophyll >5 μg L^{-1} (Figure 4c) illustrate the characteristic spatial pattern of the summer eutrophication in the PRE at that time. The notable high chlorophyll centers (>5 μg L^{-1}) were mainly confined to and most frequently (>40%) occurred in the CTZ. In addition, two distinct centers with high standard deviation (STD) of chlorophyll coexisted in the western and eastern parts of the CTZ.

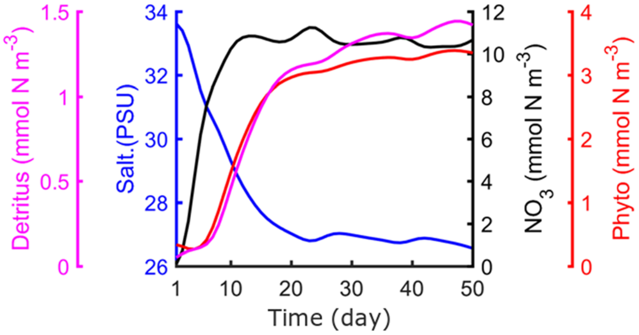

Figure 5. Time series of simulated depth-averaged salinity (Salt.), nitrate (NO_3), phytoplankton (Phyto), and detritus in the CTZ.

3.2. Persisting Hypoxia

The 10 cruises were conducted under different biophysical forcing from 2014 to 2018 (Table 1 and Figure 2). There was a strong variability in summer freshwater discharge rates among the surveyed periods, with a peak discharge rate of 37,093 m^3 s^{-1} in June 2016, which was ~5 times larger than the discharge in July 2018. Five field measurements, excluding L1 in 2015, L1–L2 in 2017, and L1–L2 in 2018, were conducted under the upwelling favorable wind conditions (i.e., the positive alongshore wind stress that blows northeastward [23° anticlockwise from true east] along the coastlines).

We observed hypoxia events during all the cruises except during L2 in 2018 when the tropical storm Son-Tinh caused intense mixing. The location and hypoxia area varied among the cruises, but almost all of the hypoxia occurred within the CTZ (Figure 2). From the cruise data, we observed that hypoxia was mainly formed in two subregions of the CTZ, dividing the CTZ into western and eastern hypoxia centers (Figure 2a). The hypoxia frequency is calculated based on the ratio between the hypoxia occurrences and the total cruise number (Figure 2b). High hypoxia frequency was observed in the entire CTZ with higher frequency (>50%) in the west and relatively lower frequency (>30%) in the east. These two hypoxia centers observed from in situ measurements geographically matched with the high surface chlorophyll centers observed from remote sensing data (Figure 4b), suggesting that hypoxia was mainly eutrophication-induced in the CTZ. In this study, we conducted the process-oriented investigation of the underlying biophysical mechanism for the eutrophication/hypoxia formation in the CTZ based on the coupled physical-biogeochemical model.

4. Model Results

4.1. Biogeochemical Response in the CTZ

Figure 5 shows how the simulated biogeochemical processes evolved in the CTZ. After the onset of the southwesterly upwelling-favorable wind on Day 1, river freshwater discharge with high nutrient loading decreased the salinity and increased NO_3 until they reached a quasi-equilibrium state after Day 20. The phytoplankton biomass bloom lagged after the sharp increase in NO_3. Due to metabolism and mortality, detritus increased as the phytoplankton and zooplankton (not shown) increased.

We averaged the simulated surface salinity, NO_3, chlorophyll, and bottom DO over a spring-neap tidal cycle from Day 38 (neap tide) to Day 45 (spring tide) and calculated the corresponding observed data and minimum bottom DO over all 10 cruises from 2014 to 2018 (Figure 6). Low-salinity surface water (<18 PSU) covered the vicinity of the river outlets and the upper and middle reaches of the PRE. The freshwater discharge had spatially asymmetric distribution with lower salinity water along the west coast because of the river outlets which are on the west coast. In addition, the Coriolis effect kept the fresher water on the western shore. Over the shelf, the northeastward wind-driven currents forced the river plume eastward. The distribution of NO_3 decreased from upper PRE (~90 mmol m^{-3}) to the entrance (~60 mmol m^{-3}) and further over the adjacent shelf (<10 mmol m^{-3}) due to the combined effect of dilution, mixing, and biological processes. The distribution patterns of simulated surface salinity and NO_3 agreed well with those from the field observations (Figure 6).

Relatively high surface chlorophyll (>10 μg L^{-1}) within the CTZ was downstream of the river outlets, and the chlorophyll concentration was relatively low in the upper and middle PRE (Figures 6e and 6f) due to light limitation and short residence time (Lu & Gan, 2015). These features are the same in the in situ

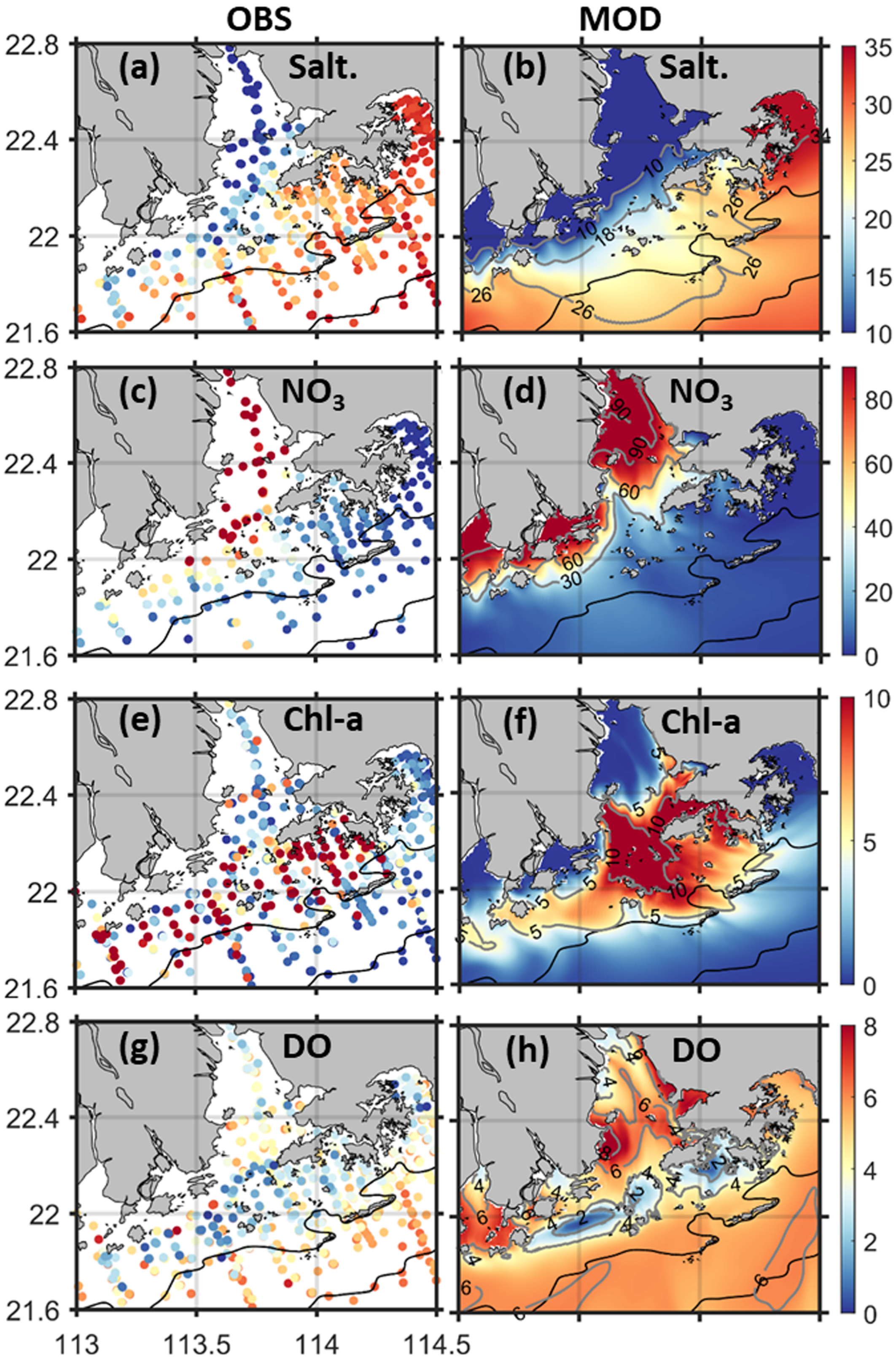

Figure 6. Horizontal distributions of the mean (a, b) surface salinity (Salt., PSU), (c, d) surface nitrate (NO_3) (mmol N m^{-3}), (e, f) surface chlorophyll (μg L^{-1}), and (g, h) minimum bottom dissolved oxygen (DO) (mg L^{-1}) from in situ measurements from 2014 to 2018 (left column) and model results averaged over a spring-neap tidal cycle (right column).

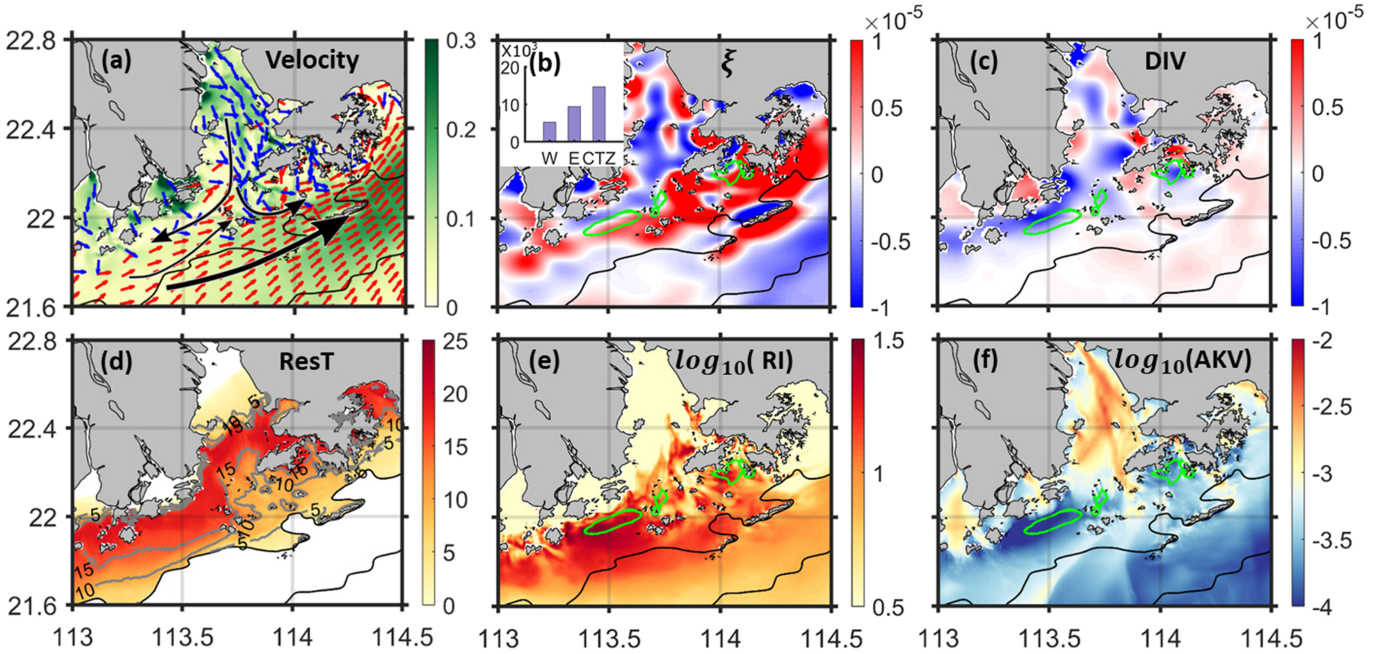

Figure 7. The simulated horizontal distributions of depth-averaged (a) velocity vectors and velocity magnitude (colored contour, ms^{-1}). The blue and red arrows represent the southward and northward flow, representatively; (b) relative vorticity (ξ, s^{-1}); The inset figure in panel (b) is Γ ($m^2\ s^{-1}$) over western, eastern, and entire CTZ; (c) divergence (DIV, s^{-1}); (d) residence time (ResT, day); (e) logarithm of the Richardson number (RI); and (f) logarithm of the vertical mixing coefficient (AKV, $m^2\ s^{-1}$). Black arrows in panel (a) show the general circulation in the PRE. Green contours in panels (b)–(f) depict the bottom hypoxia centers averaged from Day 38 to Day 45.

observations and the simulations. The most severe bottom oxygen depletion occurred underneath the surface eutrophication in the CTZ, where the two distinct hypoxia centers (<2 mg L^{-1}) occurred in the western and eastern parts. Away from the CTZ, bottom DO concentrations were relatively high (>5 mg L^{-1}) in the middle PRE and over the farther shelf region.

Overall, the eutrophication-induced hypoxia within the CTZ characterized the biogeochemical response to river plume and wind-driven upwelling circulation in the PRE. The coherent biophysical variables and hypoxia are well captured by both cruise data and our simulations, which established a level of confidence in biophysical capability of model for us to conduct the investigation of the underlying coupled physical-biogeochemical dynamics that formed hypoxia in the CTZ.

4.2. Physically Favorable Conditions for Hypoxia

The eutrophication/hypoxia in the CTZ is a combined effect of hydrodynamics and biogeochemical processes. We expected that the unique hydrodynamics would provide a biophysical-favorable environment to form eutrophication/hypoxia. The favorable environment would be characterized by the stable water column, long residence time, converging water mass, and accumulating nutrients and OM.

4.2.1. Circulation, Vortex, and Residence Time

The circulation, vortex, and associated residence time can be shown by the depth-averaged velocity vectors, ξ, and DIV in Figures 7a–7c. We filtered the tidal signals by averaging model outputs from Day 38 to Day 45. Because of the influence of variable topography, the direction and strength of the current were not spatially uniform, which led to the spatial variations in ξ and DIV. The depth-averaged currents flowed seaward from the PRE, and the shelf currents flowed mainly in the along-shore direction but veered landward to converge with the buoyant seaward jet from the PRE within the CTZ (Figure 7a). Over the shelf, the eastward upwelling jet advected the river freshwater eastward after exiting the estuary and formed buoyant and nutrient-rich plume.

Within the CTZ, the circulations formed dominant cyclonic vortices with positive ξ and convergence zones with negative DIV (Figures 7b and 7c), where the hypoxia centers occurred (green contours). The Γ (shown

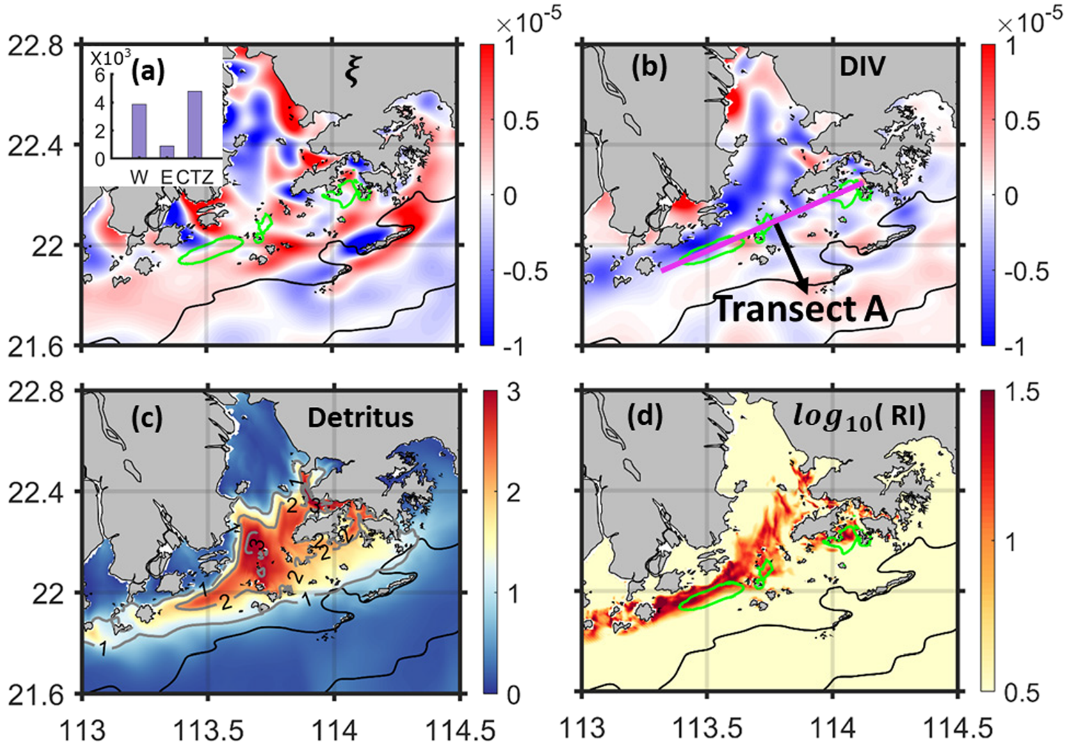

Figure 8. The horizontal distributions of the variables averaged over the bottom 2 m. (a) Relative vorticity (ξ, s^{-1}) and Γ ($m^2\ s^{-1}$, inset figure) over the western, eastern, and entire CTZ; (b) divergence (DIV, s^{-1}), (c) detritus (mmol N m^{-3}), and (d) logarithm of the Richardson number (RI). Green contours in panels (a), (b), and (d) show the bottom hypoxia zone averaged from Day 38 to day 45. Magenta line in panel (b) shows the location of Transect A in Figure 9.

in the inset chart in Figure 7b) within the western (Γ=5,389 $m^2\ s^{-1}$), eastern (Γ=10,073 $m^2\ s^{-1}$), and entire CTZ (Γ=15,462 $m^2\ s^{-1}$) shows that there were cyclonic circulations in these regions. The strongest convergence ($<-1 \times 10^{-5}\ s^{-1}$) was found at the salient edge of the western coastal cape where a seaward buoyant current and northeastward shelf current formed a cyclonic vortex over the inner shelf. Meanwhile, the high-velocity flow at the southern shelf and low-velocity flow at the lee side of the Lantau Island formed the positive ξ south of Hong Kong. These cyclonic vortices caused the convergence of the water masses.

Qualitatively similar responses occurred at the bottom. Figures 8a and 8b show that over the bottom 2 m, where hypoxia is firstly developed, ξ and DIV resembled the depth-averaged ξ and DIV. However, unlike the water-column-averaged values in Figures 7b and 7c, the bottom cyclonic circulations (positive Γ) and DIV were stronger in the western CTZ with Γ=3,876 $m^2\ s^{-1}$ and Γ=895 $m^2\ s^{-1}$ in the western and eastern CTZ, representatively.

The depth-averaged residence time (Figure 7d) of more than 15 days existed in the western CTZ and southeast of Lantau Island. The vortices-induced convergence and the long residence time of the water mass collected the nutrients and provided sufficient time for the growth of phytoplankton and sinking of detritus within the CTZ. The detritus, a result of the coagulation, mortality, and ejection of planktons based on the detritus equation, was accumulated within the bottom layer of the CTZ, as shown in Figure 8c. These physical conditions contributed to high productivity in the surface and a high abundance of OM for the consumption of DO.

4.2.2. Stratification and Mixing

In addition to the favorable circulations, vertical mixing and water column stability influence the DO. The depth-averaged Richardson number (RI) shows the relatively high RI values (>10) in the CTZ, both in the entire water column (Figure 7e) and at the bottom layer (Figure 8d). The higher RI was mainly caused the surface plume water and bottom dense seawater in the CTZ, producing a strong buoyancy frequency.

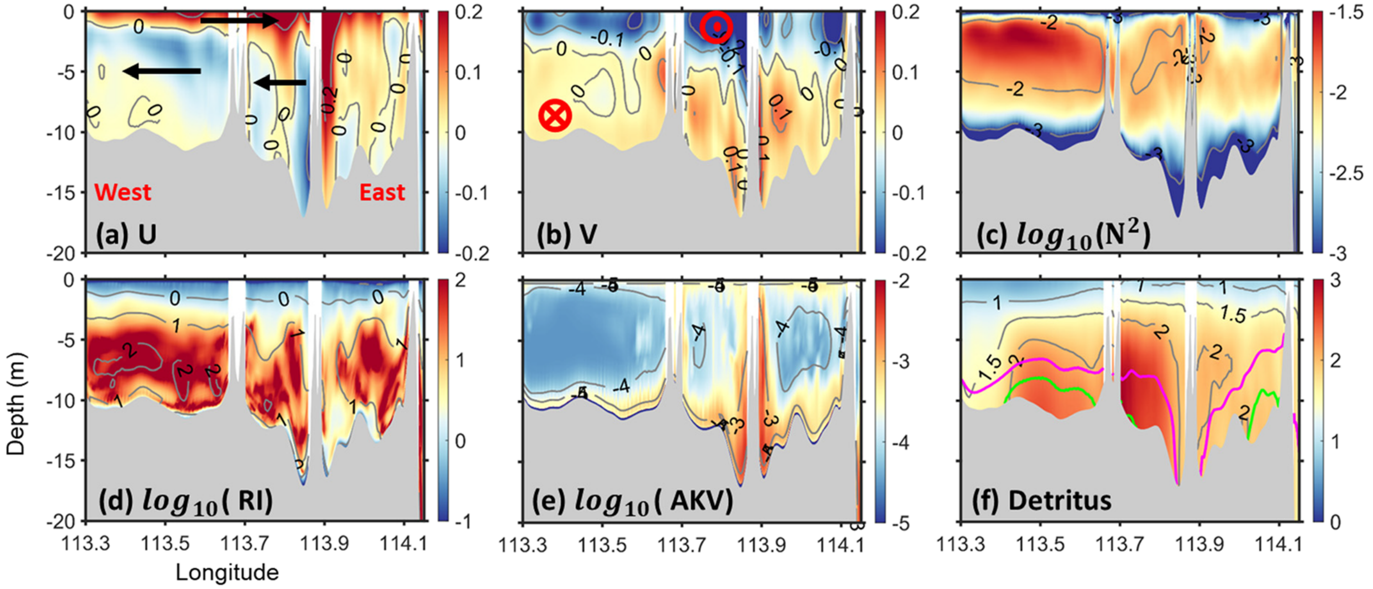

Figure 9. The vertical distributions of (a) eastward velocity (U, ms^{-1}), (b) northward velocity (V, m s^{-1}), (c) buoyancy frequency (s^{-2}), (d) Richardson number (RI), (e) vertical mixing coefficient (AKV, m^2 s^{-1}), and (f) detritus (mmol N m^{-3}) along Transect A (Figure 8b) averaged from Day 38 to Day 45. Green and magenta lines in panel (f) represent the contours of DO = 2 mg L^{-1} and DO = 4 mg L^{-1}, respectively.

Two low vertical mixing coefficient (AKV) zones, caused by the stratification suppression of turbulent mixing (Geyer, 1993), were located in the regions, particularly within the western ($<10^{-4}$ m^2 s^{-1}) and eastern zones ($<10^{-3}$ m^2 s^{-1}, Figure 7f). The more stable water column contributed to the larger HA in the western CTZ.

We also presented the response along Transect A (shown in Figure 8b) to show the vertical biophysical characteristics within the CTZ in Figure 9. The vertically sheared flows (Figures 9a and 9b) clearly reflected the three-dimensional upwelling circulation under the influence of stratification. The small N^2 ($<10^{-2}$ s^{-2}, Figure 9c) and large velocity shear (Figures 9a and 9b) with low RI (<1, Figure 9d) and high AKV ($>10^{-3}$ m^2 s^{-1}, Figure 9e) occurred in the surface boundary layer, whereas a stable regime with large RI (>10) existed in the intermediate. These physical conditions led to a high concentration of detritus (>2 mmol N m^{-3}, Figure 9f) and created a biophysical environment sufficient for hypoxia to occur along the CTZ. In particular, the relatively strong stratification and weak AKV ($<10^{-4}$ m^2 s^{-1}) were coherently found in the western and eastern hypoxia centers, while relatively strong mixing, indicated by the large AKV ($>10^{-3}$ m^2 s^{-1}), explained the relatively high bottom DO in the middle CTZ between the western and eastern hypoxia centers.

5. Biophysical Dynamics and the Hypoxia During a Tidal Cycle

5.1. Spring-Neap Cycling DO

In order to further demonstrate the coherent linkages among the currents, vortices, and biogeochemical processes in the CTZ and understand the variation of hypoxia, we examined the response of detritus, mixing, and hypoxia during the spring-neap cycle, based on both the time-series buoy data and simulation. Even though the effect of the tides on the subtidal circulation is limited compared to the effect of wind (Zu & Gan, 2015), the tidally induced circulation modulates the mixing, vortex, and resulting convergence of OM, similar to those responses to wind-driven circulation but varying within the high-frequency tidal cycle.

During a spring-neap cycle with a relatively steady wind and a slightly decreasing river discharge (Figures 10a–10c), time series measurements of vertical shear of the water column, surface and bottom density difference ($\Delta\rho$), and bottom DO from the buoy mooring (Figures 10d–10f) show that the water column was highly stratified with the $\Delta\rho$ varying from 7 to 15 kg m^{-3} at a depth of 12 m; vertical shear was very intense at the surface layer but weak vertical shear occurred at the subsurface, which led to the low DO

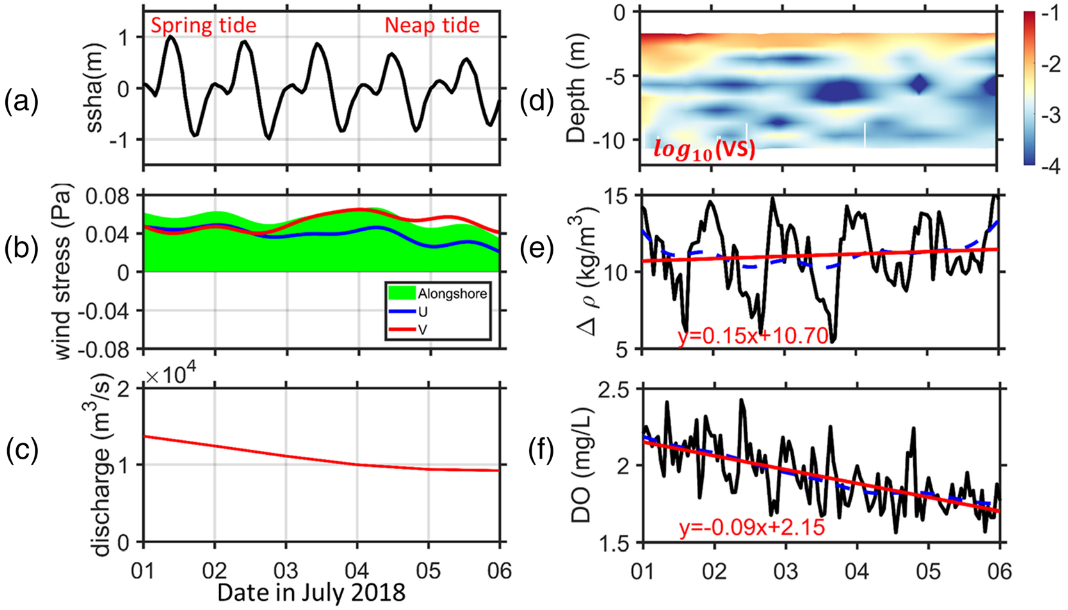

Figure 10. Time series of (a) tidal elevation at WGL, (b) wind stress at WGL, (c) river discharge, (d) logarithm of water column vertical shear (VS, s^{-2}), (e) surface and bottom density difference, and (f) bottom DO at the monitoring buoy near Hong Kong (Figure 1) from 1–6 July in 2018. The blue dashed line and red solid line in panels (e) and (f) are daily smoothed data and trends, respectively.

(~2 mg L^{-1}) at the bottom. The decreasing vertical shear (Figure 10d) and increasing $\Delta\rho$ (Figure 10e) indicate that the water column stability was enhanced from spring tide to neap tide under the steady upwelling-favorable wind (Figure 10b) in spite of the slightly declining river discharge rate (Figure 10c). At the same time, the bottom DO (Figure 10f) decreased from 2.2 to 1.7 mg L^{-1} at a rate of 0.09 mg L^{-1} day^{-1} and shows that DO was closely related to the spring-neap tidal cycle.

Similarly, simulated results show that the western and eastern hypoxia centers occurred in the CTZ during both neap and spring tides (Figure 11). The bottom hypoxia area peaked during the neap tide on Day 38 and decreased from neap to spring tide on Day 45. The spring-neap tidal current had an impact on the variation of the coupled vortex dynamics and biogeochemical processes and thus the bottom DO variation.

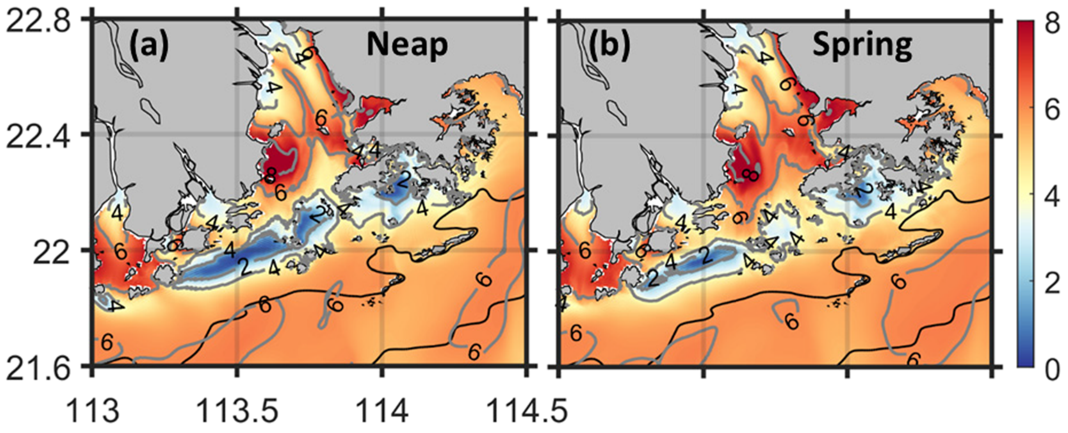

Figure 11. Horizontal distributions of simulated bottom DO (mg L^{-1}) on (a) Day 38 during the neap tide and (b) Day 45 during the spring tide.

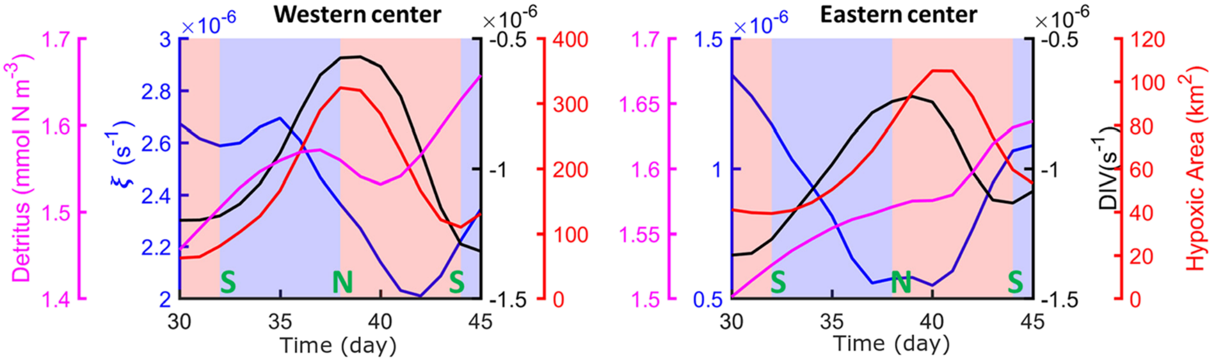

Figure 12. Time series of bottom 2 m depth-averaged vorticity (ξ, s^{-1}, blue line), divergence (DIV, s^{-1}, black line), detritus (mmol N m^{-3}, magenta line), and the hypoxia area (km^2, red line) in the western (left column) and eastern (right column) hypoxia centers. "S" and "N" refer to the spring and neap tides, respectively.

5.2. Circulation and DO Balance During Spring-Neap Tidal Cycle

Figure 12 shows the time series of bottom 2 m depth-averaged ξ, DIV, detritus, and hypoxia area within the western and eastern hypoxia centers during a spring-neap cycle. As the ocean currents were strengthening from neap to spring tide, the magnitude of ξ and DIV in these two centers were increasing, which was also amplifying the cyclonic vortices and convergence to enhance detritus accumulation. These processes are similar to those found in the subtidal current, which are favorable for the formation of hypoxia. However, unlike the subtidal current, the simultaneously enhanced mixing and vertical DO diffusion (Figure 13) had a more significant impact on weakening the hypoxia during the spring tide. As a result, hypoxia area followed the spring-neap cycle in both western and eastern centers and had a maximum area of 338 km^2 in the west and 108 km^2 in the east during the neap tide. During the spring tide, the hypoxia area decreased by 70% in the west and 51% in the east, respectively.

The time series of DO term balance from Equation 1 demonstrates the relative importance of different processes during the neap-spring cycle. Figure 13 shows the DO terms averaged over the bottom 2 m within the respective two hypoxia centers. In both hypoxia centers, the major balance was between the DO sink due to net oxygen consumption (NOC) through photosynthesis, nitrification, metabolism, and remineralization in the water column and bottom sediment and the DO source due to VDIF. The effect of HADV offsets the effect of VADV, and their difference balanced the residual of NOC and VDIF at the bottom. The relatively large NOC during the spring tide further shows that the enhanced vorticity increased the convergence of

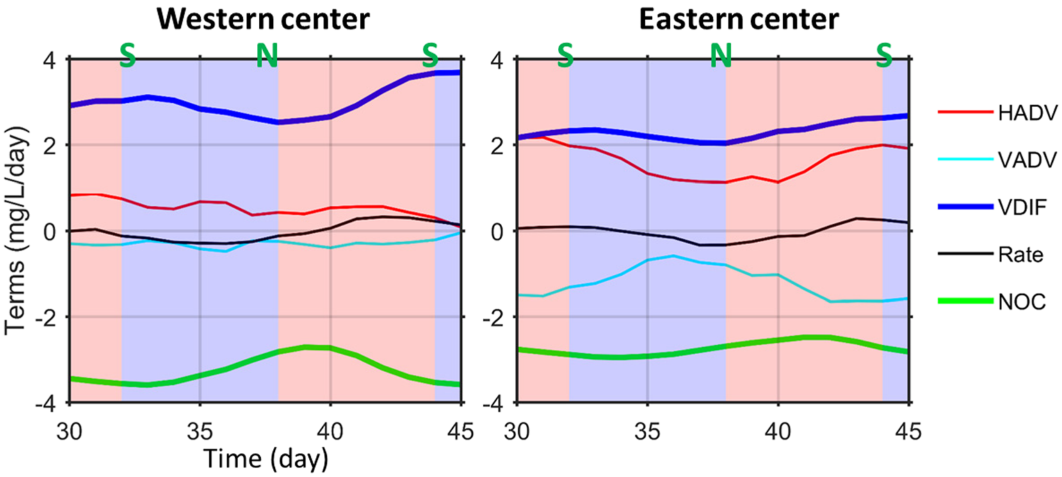

Figure 13. Time series of the DO terms from Equation 1, averaged over the bottom 2 m, in the western (left) and eastern (right) hypoxia centers. HADV: horizontal advection; VADV: vertical advection; VDIF: vertical diffusion; Rate: change rate of DO; NOC: net oxygen consumption. "S" and "N" refer to the spring and neap tides, respectively.

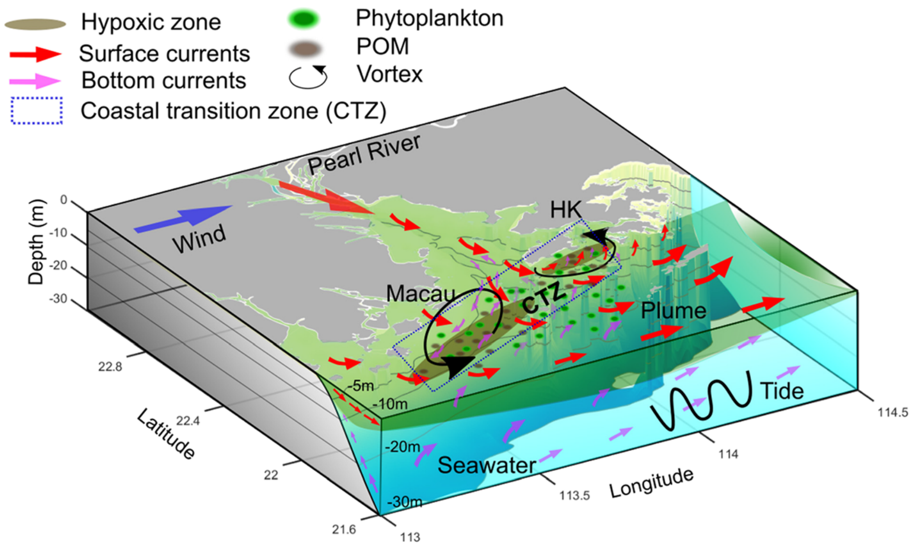

Figure 14. Conceptual model of the coupled physical and biogeochemical dynamics that control the summer hypoxia in the coastal transition zone off the Pearl River Estuary.

the OM and, subsequently, the consumption of DO, as those found in the subtidal circulation. Similarly, both the magnitudes and variations of both VDIF and NOC were much stronger in the western center than those in the eastern center, which was consistent with different magnitudes of vorticity, convergence, and detritus shown in Figure 12.

The biophysical and the bottom DO responses to spring-neap cycle further demonstrate the coherent linkages among the oceanic currents, vortex formation and convergence of OM, and the role of tidally induced mixing in the hypoxia within the CTZ. They also demonstrated that although the amplified effect of vertical DO diffusion dominated the bottom DO budget during the spring-neap cycle, the vortex dynamics associated with the subtidal circulation and biogeochemical processes determined the formation of hypoxia within the CTZ.

6. Summary and Conclusions

More and more evidence has suggested that the formation of coastal eutrophication and hypoxia is not solely determined by biogeochemical process, but by coupled physical-biogeochemical process. The coupled process is essential to determine the spatiotemporal variation of eutrophication and hypoxia that have been reported in the coastal waters around the world. In this study, we illustrated the coupled physical-biogeochemical mechanisms for the formation of hypoxia in the CTZ off the PRE based on observed data and results from a validated high-resolution process-oriented numerical model. Figure 14 sketches the summary of the physical dynamics and biogeochemical processes that caused hypoxia within the CTZ.Rich nutrients from river discharge and sufficient light stimulated the primary production and provided the necessary condition for the hypoxia to form. After exiting the PRE, the river plume flowed eastward with the wind-driven shelf current in the surface layer. The seaward flow from the PRE and shoreward veering shelf currents converged in the CTZ and characterized the zone with positive cyclonic vorticity and negative divergence and with long residence time. In particular, horizontal shear flows between the shoreward veering shelf current and seaward flowing buoyancy jet near the salient edge of the west coastal cape, and between the shelf current and the flow near the lee of Lantau Island, formed the distinct western and eastern cyclonic vortices and convergence centers in the CTZ, respectively. These hydrodynamics were favorable to cause nutrients and OM to converge and accumulate. With strong stratification and weak mixing caused by the freshwaters in the plume, the CTZ provides a biophysical environment favorable for forming hypoxia.

The biophysical processes and the bottom DO responses to the spring-neap cycle further demonstrate the coherent linkages among the oceanic currents, vortex formation and convergence of OM, and the role of tidally induced mixing in the hypoxia within the CTZ. Although the increasing VDIF in bottom DO exceed the enhanced NOC and led to a 70% and 51% decrease of HA in the western and eastern CTZ from neap to spring tide, the enhanced vorticity, convergence, and NOC during spring tide further proved the significant role of the cyclonic vortex in the transport and accumulation of nutrient and OM.

We found that the biogeochemical substances and processes provide the necessary conditions for the formation of eutrophication/hypoxia in the CTZ off the PRE. The combination of this necessary condition and unique hydrodynamic conditions that favorably strengthen biological productivity, OM accumulation, and the ensuing DO degradation provides a sufficient condition for eutrophication/hypoxia to form.

Data Availability Statement

The data used in the study are on the website https://ocean.ust.hk/data/.

Acknowledgments
This work was supported by the Theme-based Research Scheme (T21-602/16-R, OCEAN_HK project) of the Hong Kong Research Grants Council. We are grateful to the National Supercomputer Center of Tianhe-1 (Tianjin) and Tianhe-2 (Guangzhou). The model data for this study were produced by the community model ROMS (https://www.myroms.org/).

References

Breitburg, D., Levin, L. A., Oschlies, A., Grégoire, M., Chavez, F. P., Conley, D. J., et al. (2018). Declining oxygen in the global ocean and coastal waters. *Science*, *359*(6371), eaam7240. https://doi.org/10.1126/science.aam7240

Cai, W.-J., Dai, M., Wang, Y., Zhai, W., Huang, T., Chen, S., et al. (2004). The biogeochemistry of inorganic carbon and nutrients in the Pearl River Estuary and the adjacent northern South China Sea. *Continental Shelf Research*, *24*(12), 1301–1319. https://doi.org/10.1016/j.csr.2004.04.005

Chen, J., Pan, D., Liu, M., Mao, Z., Zhu, Q., Chen, N., et al. (2017). Relationships between long-term trend of satellite-derived chlorophyll-a and hypoxia off the Changjiang Estuary. *Estuaries and Coasts*, *40*(4), 1055–1065. https://doi.org/10.1007/s12237-016-0203-0

Dai, M., Gan, J., Han, A., Kung, H., & Yin, Z. (2014). Physical dynamics and biogeochemistry of the Pearl River plume. In *Biogeochemical dynamics at large river-coastal interfaces* (pp. 321–352). Cambridge: Cambridge University Press.

Diaz, R. J., & Rosenberg, R. (2008). Spreading dead zones and consequences for marine ecosystems. *Science*, *321*(5891), 926–929.

DiMarco, S. F., Chapman, P., Walker, N., & Hetland, R. D. (2010). Does local topography control hypoxia on the eastern Texas-Louisiana shelf? *Journal of Marine Systems*, *80*(1–2), 25–35. https://doi.org/10.1016/j.jmarsys.2009.08.005

Egbert, G. D., & Erofeeva, S. Y. (2002). Efficient inverse modeling of barotropic ocean tides. *Journal of Atmospheric and Oceanic Technology*, *19*(2), 183–204. https://doi.org/10.1175/1520-0426(2002)019<0183:EIMOBO>2.0.CO;2

Evans, G. T., & Garçon, V. (1997). One-dimensional models of water column biogeochemistry. *JGOFS Report*, *23*(97), 85.

Fennel, K., Wilkin, J., Levin, J., Moisan, J., O'Reilly, J., & Haidvogel, D. (2006). Nitrogen cycling in the Middle Atlantic Bight: Results from a three-dimensional model and implications for the North Atlantic nitrogen budget. *Global Biogeochemical Cycles*, *20*, GB3007. https://doi.org/10.1029/2005GB002456

Gan, J., Cheung, A., Guo, X., & Li, L. (2009). Intensified upwelling over a widened shelf in the northeastern South China Sea. *Journal of Geophysical Research*, *114*, C09019. https://doi.org/10.1029/2007JC004660

Gan, J., Lu, Z., Cheung, A., Dai, M., Liang, L., Harrison, P. J., & Zhao, X. (2014). Assessing ecosystem response to phosphorus and nitrogen limitation in the P earl R iver plume using the Regional Ocean Modeling System (ROMS). *Journal of Geophysical Research: Oceans*, *119*, 8858–8877. https://doi.org/10.1002/2014JC009951

Gan, J., Lu, Z., Dai, M., Cheung, A. Y., Liu, H., & Harrison, P. (2010). Biological response to intensified upwelling and to a river plume in the northeastern South China Sea: A modeling study. *Journal of Geophysical Research*, *115*, C09001. https://doi.org/10.1029/2009JC005569

Geyer, W. R. (1993). The importance of suppression of turbulence by stratification on the estuarine turbidity maximum. *Estuaries*, *16*(1), 113–125. https://doi.org/10.2307/1352769

Han, A., Dai, M., Kao, S.-J., Gan, J., Li, Q., Wang, L., et al. (2012). Nutrient dynamics and biological consumption in a large continental shelf system under the influence of both a river plume and coastal upwelling. *Limnology and Oceanography*, *57*(2), 486–502. https://doi.org/10.4319/lo.2012.57.2.0486

He, B., Dai, M., Zhai, W., Guo, X., & Wang, L. (2014). Hypoxia in the upper reaches of the Pearl River Estuary and its maintenance mechanisms: A synthesis based on multiple year observations during 2000–2008. *Marine Chemistry*, *167*, 13–24. https://doi.org/10.1016/j.marchem.2014.07.003

Liu, Z., & Gan, J. (2016). Open boundary conditions for tidally and subtidally forced circulation in a limited-area coastal model using the Regional Ocean Modeling System (ROMS). *Journal of Geophysical Research: Oceans*, *121*, 6184–6203. https://doi.org/10.1002/2016JC011975

Liu, Z., & Gan, J. (2017). Three-dimensional pathways of water masses in the South China Sea: A modeling study. *Journal of Geophysical Research: Oceans*, *122*, 6039–6054. https://doi.org/10.1002/2016JC012511

Liu, Z., & Gan, J. (2020). A modeling study of estuarine-shelf circulation using a composite tidal and subtidal open boundary condition. *Ocean Modelling*, *147*, 101563. https://doi.org/10.1016/j.ocemod.2019.101563

Lu, Z., & Gan, J. (2015). Controls of seasonal variability of phytoplankton blooms in the Pearl River Estuary. *Deep Sea Research Part II: Topical Studies in Oceanography*, *117*, 86–96. https://doi.org/10.1016/j.dsr2.2013.12.011

Lu, Z., Gan, J., Dai, M., Liu, H., & Zhao, X. (2018). Joint effects of extrinsic biophysical fluxes and intrinsic hydrodynamics on the formation of hypoxia west off the Pearl River Estuary. *Journal of Geophysical Research: Oceans*, *123*, 6241–6259. https://doi.org/10.1029/2018JC014199

Mellor, G. L., & Yamada, T. (1982). Development of a turbulence closure model for geophysical fluid problems. *Reviews of Geophysics*, *20*(4), 851–875. https://doi.org/10.1029/RG020i004p00851

Miles, J. W. (1961). On the stability of heterogeneous shear flows. *Journal of Fluid Mechanics*, *10*(04), 496–508. https://doi.org/10.1017/S0022112061000305

Parsons, T. R. (2013). *A manual of chemical & biological methods for seawater analysis*. Oxford: Elsevier.

Rabouille, C., Conley, D. J., Dai, M. H., Cai, W. J., Chen, C. T. A., Lansard, B., et al. (2008). Comparison of hypoxia among four river-dominated ocean margins: The Changjiang (Yangtze), Mississippi, Pearl, and Rhône rivers. *Continental Shelf Research*, *28*(12), 1527–1537. https://doi.org/10.1016/j.csr.2008.01.020

Ranasinghe, R., Turner, I. L., & Symonds, G. (2006). Shoreline response to multi-functional artificial surfing reefs: A numerical and physical modelling study. *Coastal Engineering*, *53*(7), 589–611. https://doi.org/10.1016/j.coastaleng.2005.12.004

Saulquin, B., Gohin, F., & Garrello, R. (2010). Regional objective analysis for merging high-resolution MERIS, MODIS/Aqua, and SeaWiFS chlorophyll-a data from 1998 to 2008 on the European Atlantic shelf. *IEEE Transactions on Geoscience and Remote Sensing*, *49*(1), 143–154.

Seitz, R. D., Dauer, D. M., Llansó, R. J., & Long, W. C. (2009). Broad-scale effects of hypoxia on benthic community structure in Chesapeake Bay, USA. *Journal of Experimental Marine Biology and Ecology*, *381*, S4–S12. https://doi.org/10.1016/j.jembe.2009.07.004

Shchepetkin, A. F., & McWilliams, J. C. (2005). The regional oceanic modeling system (ROMS): A split-explicit, free-surface, topography-following-coordinate oceanic model. *Ocean Modelling*, *9*(4), 347–404. https://doi.org/10.1016/j.ocemod.2004.08.002

Smolarkiewicz, P. K., & Margolin, L. G. (1998). MPDATA: A finite-difference solver for geophysical flows. *Journal of Computational Physics*, *140*(2), 459–480. https://doi.org/10.1006/jcph.1998.5901

Su, J., Dai, M., He, B., Wang, L., Gan, J., Guo, X., et al. (2017). Tracing the origin of the oxygen-consuming organic matter in the hypoxic zone in a large eutrophic estuary: The lower reach of the Pearl River Estuary, China. *Biogeosciences*, *14*(18), 4085–4099. https://doi.org/10.5194/bg-14-4085-2017

Testa, J., & Kemp, W. (2011). Oxygen—Dynamics and biogeochemical consequences. In E. Wolanski, & D. S. McLusky (Eds.), *Treatise on estuarine and coastal science* (pp. 163–199). Waltham: Academic Press. https://doi.org/10.1016/B978-0-12-374711-2.00505-2

Virtanen, E. A., Norkko, A., Nyström Sandman, A., & Viitasalo, M. (2019). Identifying areas prone to coastal hypoxia—The role of topography. *Biogeosciences*, *16*(16), 3183–3195. https://doi.org/10.5194/bg-16-3183-2019

Wei, Q., Wang, B., Yao, Q., Xue, L., Sun, J., Xin, M., & Yu, Z. (2019). Spatiotemporal variations in the summer hypoxia in the Bohai Sea (China) and controlling mechanisms. *Marine Pollution Bulletin*, *138*, 125–134. https://doi.org/10.1016/j.marpolbul.2018.11.041

Wu, J.-Z., Ma, H.-Y., & Zhou, M.-D. (2007). *Vorticity and vortex dynamics*. Berlin: Springer Science & Business Media.

Zhang, J., Wu, Y., Jennerjahn, T., Ittekkot, V., & He, Q. (2007). Distribution of organic matter in the Changjiang (Yangtze River) Estuary and their stable carbon and nitrogen isotopic ratios: Implications for source discrimination and sedimentary dynamics. *Marine Chemistry*, *106*(1–2), 111–126. https://doi.org/10.1016/j.marchem.2007.02.003

Zhao, Y., Liu, J., Uthaipan, K., Song, X., Xu, Y., He, B., et al. (2020). Dynamics of inorganic carbon and pH in a large subtropical continental shelf system: Interaction between eutrophication, hypoxia, and ocean acidification. *Limnology and Oceanography*, *65*(6), 1359–1379. https://doi.org/10.1002/lno.11393

Zu, T., & Gan, J. (2015). A numerical study of coupled estuary-shelf circulation around the Pearl River Estuary during summer: Responses to variable winds, tides and river discharge. *Deep Sea Research Part II: Topical Studies in Oceanography*, *117*, 53–64. https://doi.org/10.1016/j.dsr2.2013.12.010

Zu, T., Gan, J., & Erofeeva, S. Y. (2008). Numerical study of the tide and tidal dynamics in the South China Sea. *Deep Sea Research Part I: Oceanographic Research Papers*, *55*(2), 137–154. https://doi.org/10.1016/j.dsr.2007.10.007